UNIVERSITY OF VIRGINIA

UNDERGRADUATE SENIOR THESIS

A Full Polarization Analysis of NGC 3665

Author:
Evan Sheldahl

Supervisor:
Dr. Kristina Nyland

A thesis submitted in fulfillment of the requirements for the degree of Bachelor of Science

in the

University of Virginia Department of Astronomy

May 15, 2018

UNIVERSITY OF VIRGINIA

Abstract

University of Virginia Department of Astronomy

Bachelor of Science

A Full Polarization Analysis of NGC 3665

by Evan Sheldahl

In this thesis, I analyzed Very Large Array (VLA) L-band observations of the Stokes cube coming from the active galactic nucleus (AGN) of the lenticular galaxy NGC 3665. Its data come from the ATLAS^{3D} Survey, a highly spatially resolved dataset of 260 early type galaxies (ETGs). I present intensity maps of its non-polarized and linearly polarized emission as well as optical R-band and interferometric CO(1-0) molecular gas data. The way in which the molecular gas overlaps with the linearly polarized region suggests interactions between the radio jets and interstellar medium (ISM) are exciting the gas and yielding magnetized plasma, which in turn induces Faraday depolarization in the perceived radio emission. This provides evidence for the close links between galaxy evolution and star formation rate (SFR) being influenced by AGN feedback.

0. Contents

1. Introduction

1.1 Active Galactic Nuclei

An active galactic nucleus, simply put, is an accreting supermassive black hole (SMBH). The SMBHs found in AGN are black holes that are millions to billions of times the mass of the Sun. They are thought to exist in the centers of most galaxies, and their large gravitational fields cause them to swirl matter around them into accretion disks. The accretion of matter into the black hole leads to an expulsion of large amounts of electromagnetic (EM) radiation, which can be seen in phenomena such as radio jets and quasar winds[1]. This emission can range over the entire EM spectrum depending on the nature of the AGN. For example, dust grains surrounding an accretion disk can re-emit optical and ultraviolet photons as IR radiation, and inverse Compton scattering[2] on the accretion disk gives rise to X-ray emission (Padovani et al. 2017). AGN are very important for galaxy evolution: there is evidence of a positive correlation between SMBH mass and star formation rate (SFR) (Heckman & Best 2014), implying that accretion onto SMBHs and AGN feedback are key processes in galaxy evolution. On the other hand, AGN feedback in the form of radio jets may be responsible for the expulsion and disruption of interstellar gas, decreasing the amount of star formation in the galaxy (Morganti et al. 2013).

In this thesis, I will be talking specifically about radio emission from AGN. These radio AGN are typically powered by synchrotron emission[3] from electrons spiraling around magnetic fields produced by the rotation of the SMBH. This emission produces relativistic (moving at speeds close to the speed of light) radio jets, which usually emit in opposite directions from the center of the SMBH. The intensity of this emission as a function of frequency follows the power law

$$S \propto \nu^{\alpha} \tag{1.1}$$

where α is the spectral index (Condon 1992), S is the intensity, and ν is the frequency.

Radio galaxies have historically been classified as FR-I or FR-II type, a classification given by Fanaroff & Riley (1974). The main difference between FR-I and FR-II galaxies is the distribution of their brightness. Fanaroff and Riley use the ratio R_{FR}, which is the ratio of the distance across the brightest contour outside the central AGN over the distance across the lowest brightness contour. FR-I galaxies have a R_{FR} ratio less than 0.5, and are therefore core-brightened. FR-II galaxies have a R_{FR} greater than 0.5, and are therefore edge-brightened. In terms of total luminosity, the

[1]A quasar is an AGN of incredibly high luminosity, typically made of energetic jets emitting frequencies all across the EM spectrum. The brightest quasars can reach luminosities of around $10^{3}4ergss^{-1}$.

[2]Inverse Compton scattering is the scattering of photons by charged particles, increasing the photon's energy

[3]Synchrotron emission is emission from relativistic charged particles spiraling around magnetic field lines (Padovani et al. 2017)

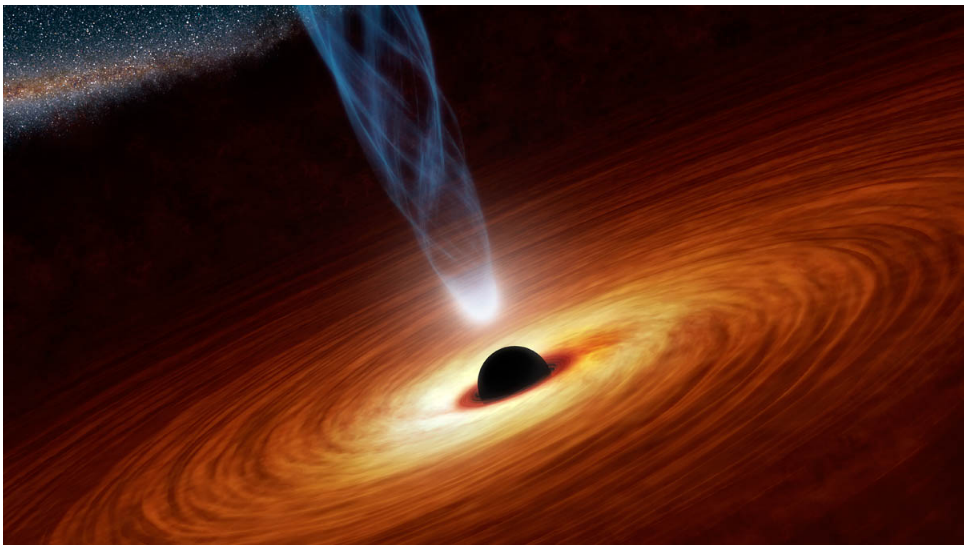

FIGURE 1.1: Artist's depiction of an AGN, an accreting black hole emitting relativistic jets.

radio sources in FR-II galaxies tend to be brighter than in FR-I galaxies. Figures 1.2 and 1.3 below depict examples of FR-I and FR-II galaxies, respectively.

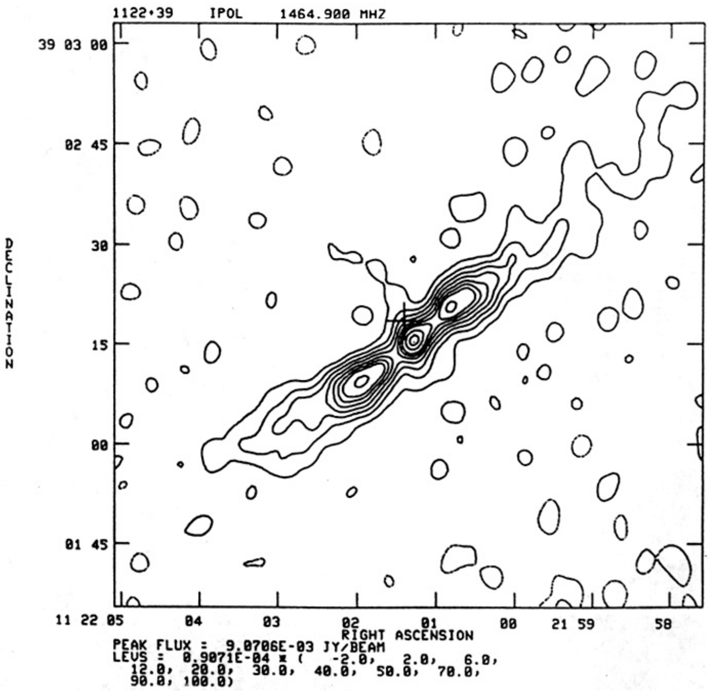

FIGURE 1.2: A VLA radio image of NGC 3665 from Parma et al. (1986). This depicts an example of an FR-I radio galaxy. The restoring beam is about 3.5 arcsec. The levels are in Jy/beam. Notice the high flux density central region and diffuse outer regions.

1.1.1 Polarization

Polarization is when the oscillation of a transverse EM wave is in only a specific plane. For light, which is an EM wave, this means that it is composed of electric

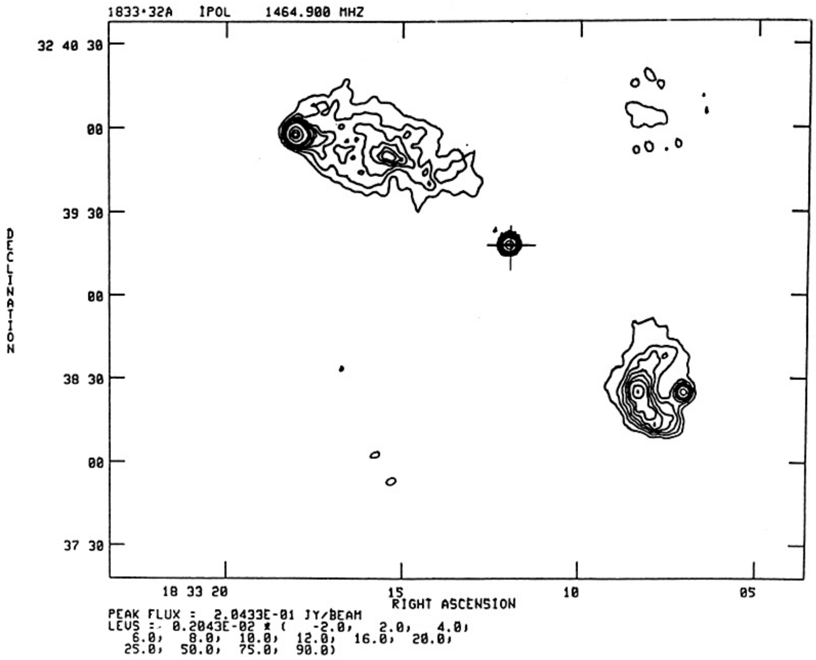

FIGURE 1.3: A VLA radio image of B2 1833+32A from Parma et al. (1986). This depicts an example of an FR-II radio galaxy. The restoring beam is about 3.5 arcsec. The levels are in Jy/beam. Notice the radio lobes with high flux density and the diffuse region between the lobes and the center.

field waves traveling in tandem with magnetic field waves oscillating orthogonal to the electric field. In radio astronomy, the polarization typically refers to the orientation of the electric field wave. This is because radio telescopes are only sensitive to electric field waves. Synchrotron radiation in radio jets emits polarized light due to the orderly motion of the charged particles in the jets. This is because the angle of polarization is parallel to the direction of the magnetic field line the emitting particle is spiraling around (Rybicki & Lightman).

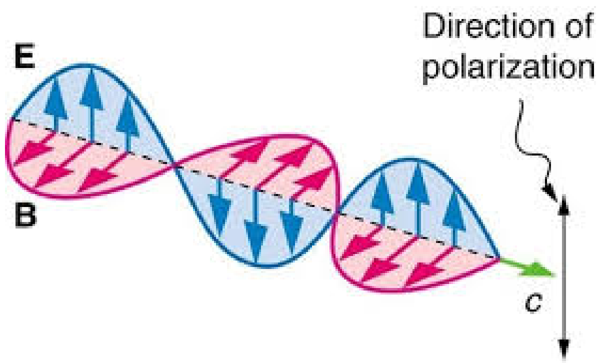

FIGURE 1.4: A depiction of a polarized EM wave. Credits: quora.com.

The linear polarization properties of an EM wave can be described by the Stokes parameters Q and U. The four Stokes components (IQUV) individually represent the total intensity, horizontally/vertically polarized light, $\pm 45°$ polarized light, and circularly polarized light, respectively. Their equations are given by

$$I = A_x^2 + A_y^2 \tag{1.2}$$

$$Q = A_x^2 - A_y^2 \tag{1.3}$$

$$U = 2A_x A_y cos(\delta_{xy}) \tag{1.4}$$

$$V = 2A_x A_y sin(\delta_{xy}) \tag{1.5}$$

where A_x and A_y are the amplitudes of the electric field in the x and y direction, and $\delta_{xy} = \delta_x - \delta_y$, the phase difference between the x and y electric field waves (Brentjens 2014). The electric field wave is given by the formula

$$E_{x,y} = A_{x,y} cos(2\pi \nu t + \delta_{x,y}) \tag{1.6}$$

The total linear polarization intensity is simply the magnitude of the two linearly polarized Stokes parameters.

$$P = \sqrt{Q^2 + U^2} \tag{1.7}$$

The polarization fraction is the ratio of the total linear polarization P and Stokes I. The polarization angle Φ can be calculated by taking the inverse tangent of the fraction of the Stokes Q and U.

$$\Phi = \frac{1}{2} \arctan \frac{U}{Q} \tag{1.8}$$

These polarization angles are under the influence of Faraday rotation, which can affect the polarization of radio jets. This happens when synchrotron emission plows through magneto-ionic material along the jet's line of sight, rotating its angle of polarization (O'Sullivan et al. 2017). When this reduces the degree of polarization in the observed radiation, it is called Faraday depolarization. The angle of rotation that Faraday polarization effects induce on this radiation is the rotation measure (RM). By analyzing the polarization angles of radiation emitted from AGN, one can quantify the amount of Faraday depolarization and therefore learn more about the interaction between radio jets and the surrounding medium causing the depolarization.

1.1.2 NGC 3665

NGC 3665 is a lenticular galaxy[4] in the constellation Ursa Major. It has a prominent dust lane, which is almost perpendicular to its radio jets (Parma et al. 1986). It is an FR-I type radio AGN. It is also a jet-mode AGN, meaning the majority of its radiated emission comes from its radio jets rather than radiative emission from the SMBH accretion disk. Also characteristic of jet-mode AGN, it has a large SMBH mass $5.75^{+1.49}_{-1.18} \times 10^8 M_\odot$ and low X-ray luminosity compared to its Eddington limit ($log(L_X/L_{Edd}) = -6.73$) (Onishi et al. 2017). Its X-ray luminosity is used here because it is the best prediction of its bolometric luminosity. It is unique in that it has a dynamical black hole mass measurement, meaning it is based on measurements of the black hole's kinematics rather than predictions using scaling relations (Kormendy and Ho, 2013). NGC 3665 is located at RA = 11h24m43.672s, Dec = +38°45′46.27" in J2000 coordinates (Evans et al. 2010) and a distance of 33.1 Mpc away (Cappelari et al. 2011), which gives it a scale of ~31.158 (arcsec/5 kpc). Its

[4] Lenticular galaxies are bulge-dominated galaxies that also contain a disk component

total stellar mass is $10^{1}1.56 M_{\odot}$ (Nyland et al. 2016). There is also a collection of CO and H_2 molecules surrounding its core (Fig. 1.6). This H_2 gas has a total mass of $10^{9.11 \pm 0.01} M_{\odot}$ (Alatalo et al. 2013). It has bright Stokes I emission throughout the center while it has pronounced linearly polarized emission from its two radio jets.

FIGURE 1.5: An optical image of NGC 3665. Credits: Pan-STARRS Herschel 3-π stacked survey.

The ATLAS^{3D} Survey includes multi-wavelength data of 260 early type galaxies (ETGs) within 42 Mpc of Earth and brighter than -21.5 in absolute magnitude (Cappellari et al. 2011). The goal of the survey is to classify ETGs based on global stellar kinematics and try to discern the nature of their formation and evolution. NGC 3665 is one of the galaxies included in the ATLAS^{3D} Survey, and is also one of the few galaxies to have extended radio jets that have been spatially resolved.

1.1.3 The VLA

The Very Large Array (VLA) is a radio interferometer that began construction in 1973 and was formally dedicated in 1980. It is an array of 27 radio telescopes, each with a diameter of 25 m, located in the Plains of San Agustin near Magdalena, New Mexico. It detects radio emission over a range of 73-50,000 MHz (0.073-50 GHz) with a resolution ranging from 0.043" (at 45 GHz) to 850" (at 0.074 GHz). It does this by measuring the electric field of incoming radio waves. An interferometer uses multiple telescopes to discretely sample a single telescope of large aperture, this aperture being the size of the longest distance between two telescopes, also known as the baseline. Unlike some interferometers, it has four configurations: A, B, C, and D. These configurations have baselines of 36.4, 11.1, 3.4, and 1.03 km, respectively. Larger baselines yield higher angular resolution but lower surface brightness sensitivity.

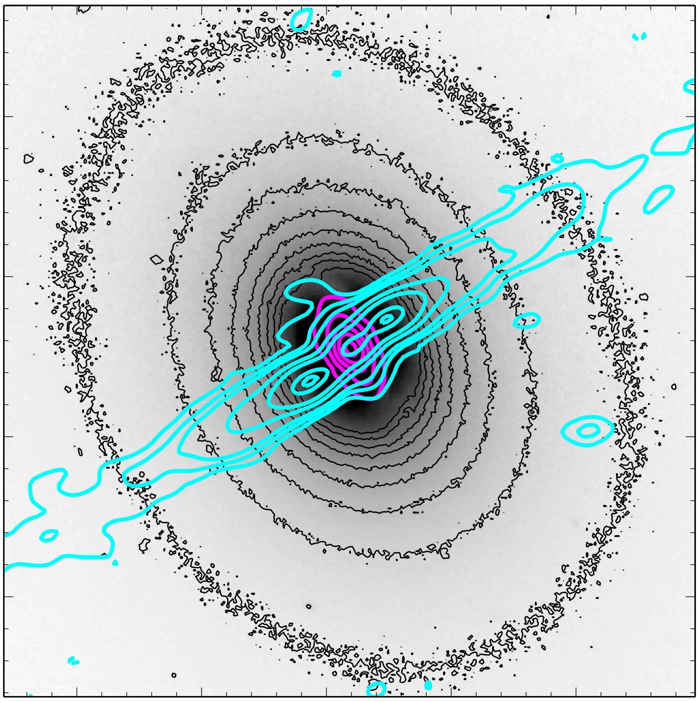

FIGURE 1.6: An R band optical map of NGC 3665 with 1.5 GHz Stokes I contours (Nyland et al. 2017) in cyan and CO(1-0) emission (Alatalo et al. 2013) in magenta.

FIGURE 1.7: A photograph of the VLA in one of its four configurations. Credits: images.nrao.edu.

2. Data Analysis

2.1 Methods

Data reduction was performed with version 5.1.1-5 of the Common Astronomy Software Applications (CASA; McMullin et al. 2007) software package. This data analysis section generally follows the steps laid out by CASA Guides' VLA Continuum Tutorial 3C391[1] for CASA Version 4.6 or later. All references to programs used for data reduction are part of this package, and are referred to in all caps (e.g. plotcal() = PLOTCAL).

2.2 Observations

The relevant observations referenced in this thesis are detailed in Table 2.1. The project ID is 10C-173. They were taken in the L-band (1-2 GHz) from 55651.005127 to 55651.21291 MJD (March 31, 2011, 00:07:23.0 to 05:06:35.4 UTC) while the VLA was in the B configuration.

Source	Field ID	Purpose
3C84	0	Leakage calibrator
J1130+3815	6	Complex gain calibrator
3C286	18	Bandpass, flux density scale, pol angle calibrator
NGC3665	7	Target source

TABLE 2.1: Observed sources.

2.3 Flagging

FLAGDATA was used to remove bad data from the measurement set. I flagged the first scan due to it being a dummy "set-up" scan. In addition, the first six seconds of each scan were also "quack" flagged[2]. Through additional inspection in PLOTMS, I identified two malfunctioning antennas (ea17 and ea25) that I ultimately removed from the dataset manually using FLAGDATA. Ea12 was selected as the reference antenna due to its close proximity to the center of the array and low percentage of flagged data.

[1]https://casaguides.nrao.edu/index.php/VLA_Continuum_Tutorial_3C391-CASA4.6

[2]Quack flagging is the practice of flagging the beginning of each scan to account for the antenna needing to "settle" before the data can be considered accurate

2.4 Calibration

After flagging, the measurement set was hanning smoothed using HANNINGSMOOTH with the parameter datacolumn='data' in order to remove the Gibbs ringing effect[3] from the main data. I then used GENCAL for a priori antenna position corrections (caltype='antpos'). Then, I executed SETJY on the flux calibrator for in order to set the flux density as a function of frequency to be used throughout the rest of calibration. This was done using the scale from Perley & Butler (2013) and the L-band VLA standard model for 3C286. I then used GAINCAL for initial phase calibration (calmode='p') and antenna-based delay calibration (gaintype='K') on 3C286 using the parameters solint='inf', minsnr=5, and spw='*27∼36'. I included the a priori antenna position correction in the parameter caltable for initial phase calibration, then used both the antenna position and initial phase calibrations in caltable for the antenna-based delay calibration. The purpose of the initial phase calibration was to average over the variations in phase over time in the bandpass. This way, the bandpass calibration would be more accurate. Antenna-based delay calibration accounts for other antennas not being in sync with the reference antenna. I used BANDPASS to solve for the complex bandpass to account for the variation of gain[4] with frequency. This was run with the parameters solint='inf' and combine='scan' in order to combine and average the solutions for all scans, as well as bandtype='B' for solving for bandpass for each channel. I included all previous calibration solutions in the caltable. Next, I used GAINCAL again to calculate how the complex antenna gains varied over time. This was run for fields 0, 6, and 18 (the leakage, complex gain, and bandpass calibrators, respectively) with parameters gaintype='G', solint='inf', calmode='ap' (to solve for amplitude and phase), solnorm=False, and interp=['nearest','nearest','nearest']. The parameter caltable included the antenna position correction, the antenna-based delay calibration, and the complex bandpass solution.

2.4.1 Polarization Calibration

For the polarization calibration, I calculated the spectral index α in order to create a polarized flux model using SETJY. This was done using the formula

$$\alpha = log(S_0/S_1)/log(\nu_0/\nu_1) \tag{2.1}$$

In which the S_n and ν_n are the flux and central frequency of the nth spectral window, respectively. This equation comes from taking the logarithm of both sides of Eqn. 1.1. Using info from Perley & Butler (2013) gives us $\alpha = -0.50051$. The flux in spectral window 0 and channel 0, $S_0 = 14.897$ Jy, was used as a reference flux. I also used $c_0 = 0.095000$ for a fractional polarization of 9.5% and a polarization angle of $d_0 = 0.57596$ radians (33°) at a reference frequency of 1.45 GHz.

$$P_0 = I_0 \times c_0 \tag{2.2}$$

$$Q_0 = P_0 \times cos(2 \times d_0) \tag{2.3}$$

$$U_0 = P_0 \times sin(2 \times d_0) \tag{2.4}$$

[3]Gibbs ringing is an effect where there is a "ringing pattern" around sharp frequency changes in the Fourier spectrum due to a finite number of Fourier components approximating a delta function

[4]Gain is amplification or sensitivity of the input electronic signal

The factor of two in Eqn. 2.3 and 2.4 comes from the sum of the polarization angles d_0 of both the Q and U planes. I plugged these parameters into SETJY to give results for the fractional polarization intensity, Stokes Q, and Stokes U intensities for the first two spectral windows (signified by subscript) of 3C286.

Quantity	Name	Value
I_0	Stokes I Intensity	15.955
P_0	Fractional Polarization Intensity	1.516
Q_0	Stokes Q Intensity	0.617
U_0	Stokes U Intensity	1.385
I_1	Stokes I Intensity	15.209
P_1	Fractional Polarization Intensity	1.445
Q_1	Stokes Q Intensity	0.588
U_1	Stokes U Intensity	1.320

TABLE 2.2: The measurements of the Stokes cube and fractional polarization intensities of 3C286 for n=0,1, given in Jy.

The Stokes I is composed of RR and LL polarization correlations, or the parallel polarization components. For polarization calibration, I had to next solve for the RL and LR, or cross hand, components. I did this by using GAINCAL to accounts for the delay differences on the reference antenna between the right and left components. Once again, 3C286 was used for reference fluxes because its polarization properties are well known. I used the parameters parang=True, spw='*5∼58", and gaintable including the antenna position correction, antenna-based delay calibration, the complex bandpass solution, and the complex gain calibration.
After that, I calibrated out the instrumental polarization, or "leakage terms," on all previous calibration solutions by using POLCAL with 3C84, using parameters spw='*5∼58', poltype='Df', solint='inf', combine='scan', and gaintable including the antenna position correction, antenna-based delay calibration, the complex bandpass solution, the complex gain calibration, and the cross-hand delay solutions. Upon calibration, I encountered more bad data and removed them using FLAGDATA with the parameter mode='rflag', an automatic RFI algorithm, on the fields 0, 6, 7, and 18. Next, I solved for the R-L polarization angle using POLCAL. This corrected the phase between the R and L components. This was accomplished by using the parameter poltype='Xf', for a frequency-dependent position angle calibration, as well as a gaintable including all the previous files used in the gaintable when correcting for the leakage terms, plus the resulting leakage corrections. In addition, I set mean amplitude gains of fields 0 and 6 equal to that of field 18 using FLUXSCALE. This was done with incremental=False in order to apply the scaling factors directly to the resulting gaintable instead of outputting a separate table with flux scaling factors. The caltable I used was the antenna-based delay calibration. Finally, these calibration solutions were applied to all relevant fields using APPLYCAL to produce a calibrated data set to begin imaging.

2.4.2 Initial Imaging

For the full polarization imaging, the calibrated measurement set was formed into a single image cube containing all four Stokes planes (IQUV) using CLEAN. Some of the custom parameters I used were threshold='0.03mJy', weighting='briggs', nterms=1, and multiscale=[0,5,15]. A threshold of 0.03 mJy was used as the minimum flux level at which to stop cleaning because it is close to the ideal noise level of

0.02 mJy. Briggs weighting was used the dataset did not require specifically natural or uniform weighting, so I used Briggs weighting to include the benefits of both. The different scales for multiscale were chosen to roughly correlate to one and three times the size of the beam, which are about the sizes of one of the higher Stokes I brightness contours and the extent of the central AGN, respectively. A primary beam (PB) correction was applied using IMPBCOR. I then used IMSUBIMAGE to split the full-polarization Stokes cube into four images, one of each Stokes plane. The Stokes planes Q and U were combined using IMMATH to form the linear polarization map, using a σ_{rms}[5] of 0.022 mJy/beam. This was then PB corrected as well. Next, I used IMMATH to create polarization angle and fractional linear polarization maps. However, it became apparent that more phase and amplitude calibration was necessary, as there were significant sidelobe patterns in and around the Stokes I image of the AGN.

2.5 Self-Calibration

The data had to undergo multiple trials of phase and amplitude self-calibration in order to eliminate the sidelobe patterns and reduce the background noise. To begin, I ran the dataset through the CLEAN algorithm with the parameters cell = '0.75 arcsec', threshold='0.02mJy', weighting='briggs', nterms = 1, and multiscale=[0,6,10]. This was in order to create a "template" for GAINCAL to act on. I ran GAINCAL in calmode = 'p' for a variety of solution intervals (from largest to smallest, solint='120s', '60s', '30s', '15s', '10s'). After gain solutions were calculated with GAINCAL, I ran APPLYCAL to apply the solutions to the dataset. This was first done for GAINCAL(solint='60s'), interp = 'nearest'. Once applied with APPLYCAL, I ran CLEAN again to produce a new Stokes cube with these solutions. I repeated this process for solint='30s', as well as changed the parameter threshold in CLEAN to '0.025mJy'. After that, I did the process again for solint='15s'. This concluded the phase calibration segment of the self-calibration, and for later runs of GAINCAL I set calmode='a' for amplitude calibration.

After running CLEAN again for solint='15s' after applying an amplitude calibration with GAINCAL, I tweaked the mask used for CLEAN to better encompass point sources. Furthermore, repeated phase and amplitude calibration increased the confidence of the emission around the AGN of NGC 3665 of being real, so I extended the mask around the AGN to better match the real emission found in the residual image. At this point, I also changed the multiscale parameter in CLEAN from [0, 6, 10] to [0, 6, 18] in order to better reflect the scales of the lobes of the AGN. After one more reduction of solint to '10s' and more tweaking of the mask, I produced the final fully calibrated Stokes cube for NGC 3665.

2.5.1 Final Imaging

To create the final image, I largely followed the same steps in Section 2.4.2. To create the polarization intensity map, I used IMSUBIMAGE to split out the different Stokes axes from the calibrated full polarization Stokes cube, as well as an additional primary-beam corrected Stokes I. Then, to create the linear polarization map, I used IMMATH to combine the Stokes Q and U images into a full linear polarization image

[5] σ_{rms} is the RMS noise, which is the root mean square of the electronic signals coming from sources other than the target field

(Eqn 1.7). I applied a primary-beam correction to that image by using IMSUBIMAGE to extract the Stokes Q flux file (this is the same as the Stokes U flux file, so they can be used interchangeably) from the full polarization flux image, then applying it to the full polarization image with IMMATH. This combining of images was done using the formula

$$IM_0[IM_1 > 0.1]/IM_1 \tag{2.5}$$

where IM_0 is the full polarization intensity image and IM_1 is the flux for Stokes Q. The threshold 0.1 mJy/beam was chosen because it is roughly five times the uncertainty σ_{rms} of 0.02 mJy/beam used earlier for the threshold parameter in CLEAN. To make the polarization angle map, I used IMMATH with mode = 'pola' for polarization angle (Eqn. 1.8).

3. Results

Figures 3.1 and 3.2 depict various intensity maps of NGC 3665, showing off the non-polarized and linearly polarized features of the AGN. Figures 3.4a - 3.4d are the four Stokes planes of NGC 3665, while Figures 3.5a - 3.5c showcase the linear polarization of NGC 3665. For all figures, the beam size is 6.68923 by 3.82689 arcsec (semi-major axis by semi-minor axis). In Figure 3.3, these are the parameters for the leftmost beam used for the Stokes I and linearly polarized data. The rightmost beam is used for the CO contours and has a beam size of 4.25796 by 4.15668 arcsec (semi-major axis by semi-minor axis).

Figure 3.1 is of a Stokes I map of NGC 3665 with Stokes I contours. Here you can clearly see a bright central region, indicative of FR-I galaxies, with prominent radio jets being expelled about $\pm 45°$ from the source, a sign of jet-mode AGN. There is a small amount of visible emission orthogonal to the plane of the jets, which is likely CO(1-0) from a molecular gas cloud (see Figure 1.6). The effects of this gas cloud can be seen in Figure 3.2, which shows the linearly polarized flux with Stokes I contours and polarization fraction vector overlays. Another view of this is given in Figure 3.3, depicting the linearly polarized flux, Stokes I contours (same as in Figure 3.2) in cyan, and CO(1-0) contours in magenta. Notice the lack of linear polarization in the center in the region outlined by the molecular gas. This is evidence that the molecular gas is reducing the degree of polarization of the radio emission coming from that region through Faraday depolarization. I will need to conduct further research to quantify the RM along the AGN.

Figures 3.4a - 3.4d depict the four Stokes planes of NGC 3665, showing non-polarized, linearly polarized, and circularly polarized emission. I did not detect any circular polarization from NGC 3665, which is why Fig 3.4d is primarily noise. Figures 3.5a - 3.5c depict the linear polarization properties of NGC 3665, including the total polarized flux (see Equation 1.7), the linear polarization fraction, and the polarization angle map. Consistent with our other measurements, Figure 3.5b shows its minimum linear polarization fraction in the center, and Figure 3.5c has a region in the center where the linear polarization angle is closest to zero.

Circular polarization can be represented as a superposition of two waves of linearly polarized light orthogonal to each other and out of phase. If the two linear waves are perfectly in phase (e.g. when $\delta_{xy} = 0$), then V = 0. I did not detect any circularly polarized light from NGC 3665. From the Q and U components of NGC 3665, I calculated the full polarization intensity (Figure 3.5a), which simply contains the intensity of the linear polarization of NGC 3665, and the polarization angle map (Figure 3.5c), which contains the angles of the planes of polarization at various points around the AGN. These polarization angles are under the influence of Faraday rotation.

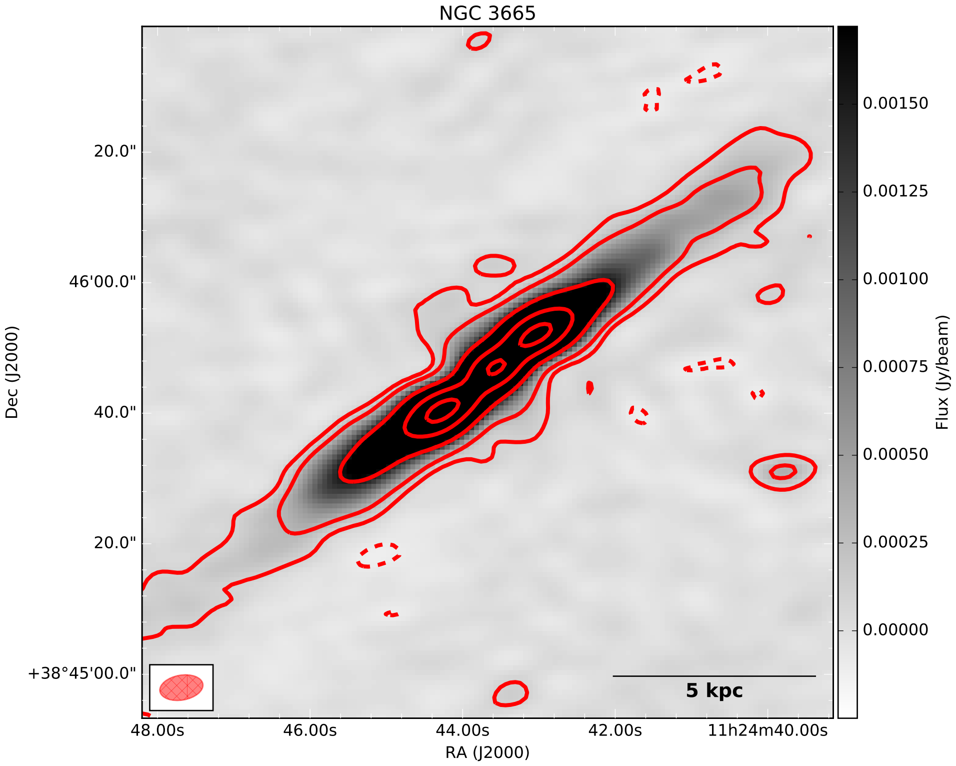

FIGURE 3.1: A linear polarization intensity map of NGC 3665 with Stokes I contours. The unit contour level is the same as the RMS noise: 30.8 μJy beam^{-1}, Relative Contours: [-3, 3, 10, 50, 150, 280].

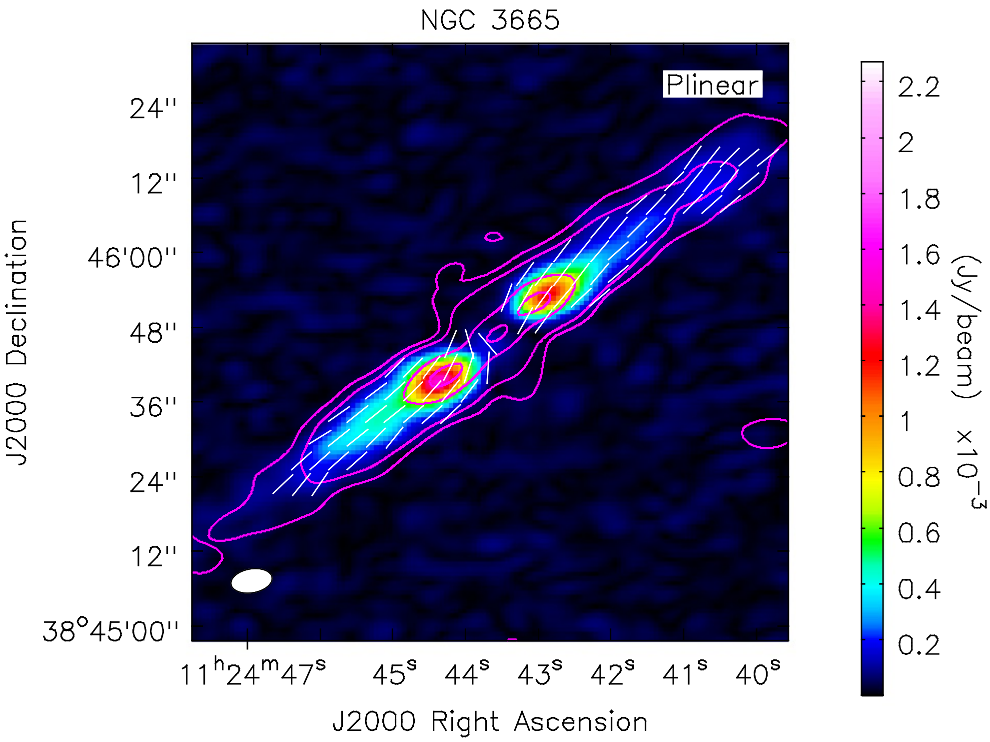

FIGURE 3.2: A linear polarization intensity map of NGC 3665 with Stokes I contours and polarization fraction vectors. The unit contour level is the same as the RMS noise: 30 μJy beam^{-1}, Relative Contours: [-1.1, 1.1, 1.4, 5, 10, 20, 35, 50].

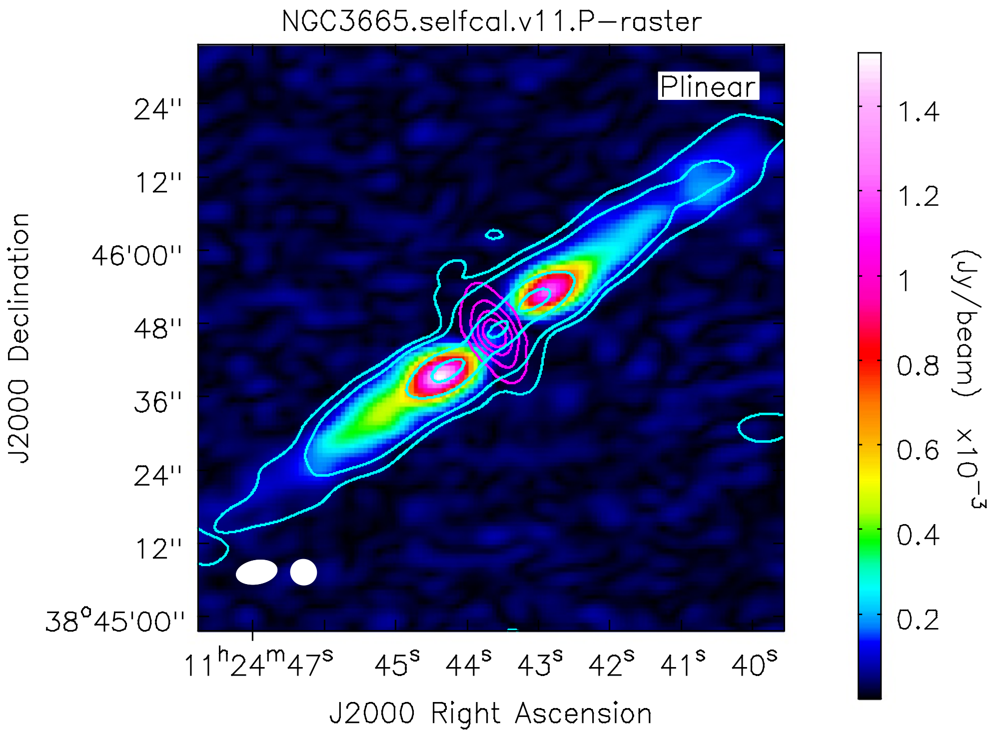

FIGURE 3.3: A linear polarization intensity map of NGC 3665 with Stokes I contours in cyan and CO(1-0) contours in magenta. The leftmost beam is used for the intensity map and Stokes I contours. The rightmost beam is used for the CO contours. The unit contour level is the same as the RMS noise: 35.0 μJy beam^{-1}, Relative Contours: [-1.1, 1.1, 1.4, 5, 10, 20, 35, 50].

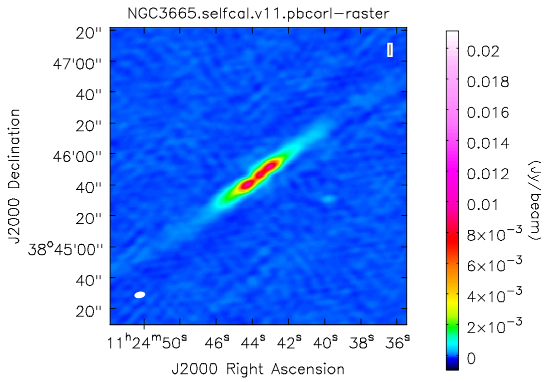

(A) A PB corrected Stokes I map for NGC 3665. The colorbar is in units of mJy/beam. The RMS noise is 2.336×10^{-5} Jy/beam. The integrated flux is 5.851×10^{-4} Jy. The maximum flux is 1.003×10^{-2} Jy/beam.

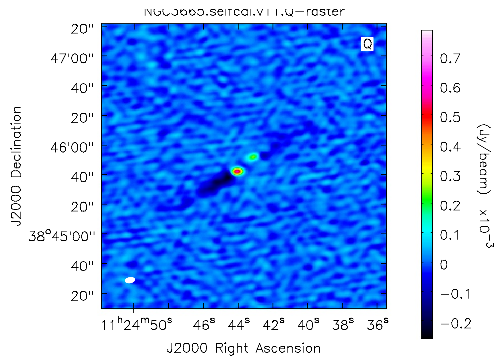

(B) A Stokes Q map for NGC 3665. The RMS noise is 1.975×10^{-5} Jy/beam. The integrated flux is -6.795×10^{-4} Jy. The maximum flux is 5.894×10^{-4} Jy/beam.

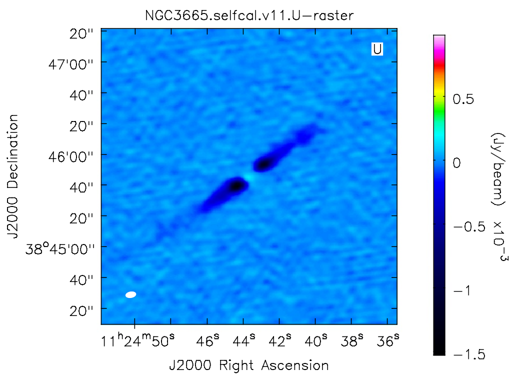

(C) A Stokes U map for NGC 3665. The RMS noise is 1.994×10^{-5} Jy/beam. The integrated flux is -9.326×10^{-3} Jy. The maximum flux is 1.654×10^{-4} Jy/beam.

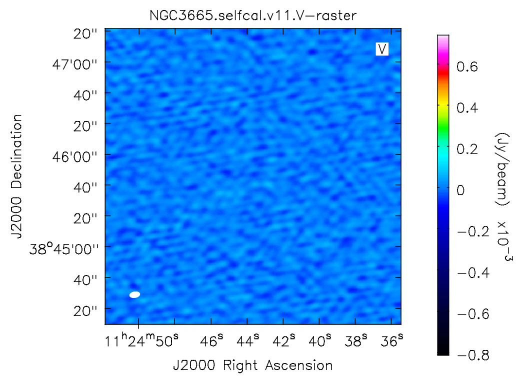

(D) A Stokes V map for NGC 3665. The RMS noise is 2.219×10^{-4} Jy/beam. The integrated flux is 2.671×10^{-4} Jy. The maximum flux is 6.511×10^{-5} Jy/beam.

FIGURE 3.4: Stokes cube images for NGC 3665.

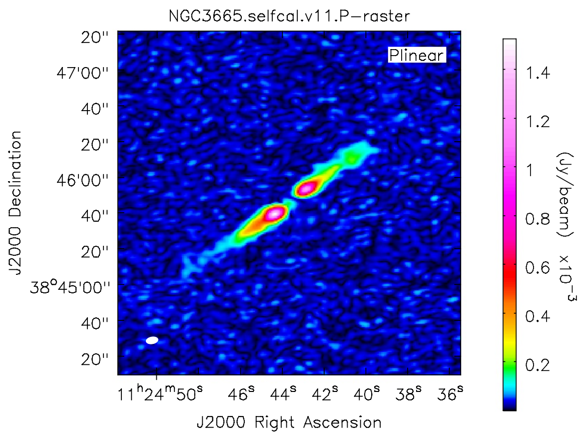

(A) A total linear polarization (P) map for NGC 3665. The RMS noise is 2.808×10^{-5} Jy/beam. The integrated flux is 1.161×10^{-2} Jy. The maximum flux is 1.529×10^{-3} Jy/beam.

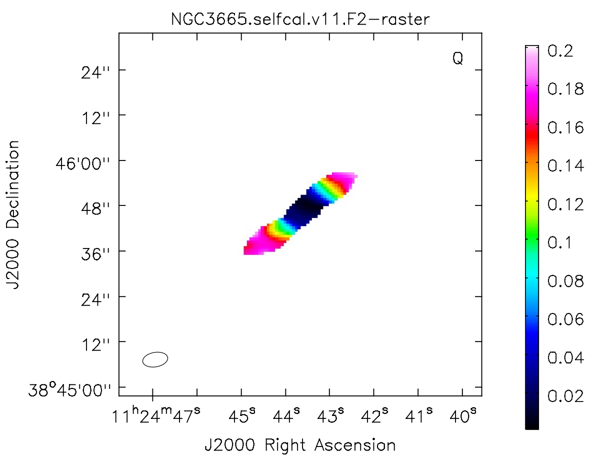

(B) A fractional linear polarization (F) map for NGC 3665. The RMS noise is 1.910×10^{-1}. The range of polarization fraction values is 3.928×10^{-3} to 2.014×10^{-1}. The mean polarization fraction is 1.009×10^{-1}.

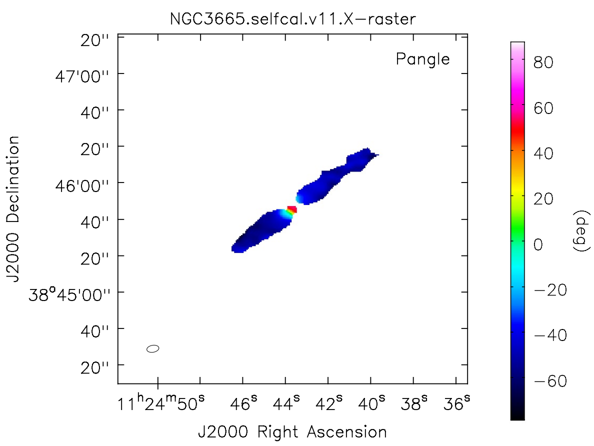

(C) A polarization angle (X) map for NGC 3665. The RMS noise is 49.743°. The range of the polarization angle is -71.176° to 54.143°. The mean polarization angle is -46.698°.

FIGURE 3.5: Linear polarization images for NGC 3665.

4. Discussion

My results may be evidence of AGN feedback affecting star formation and galaxy evolution. Visible in Figures 1.6 and 3.3 is a central molecular gas cloud made of gas responsible for star formation. This gas spatially coincides with the radio jets as seen in Figures 3.3, 3.5b, and 3.5c. My measurements of the core fractional linear polarization are less than 1.6%, in line with the 20 cm (1.5 GHz, L-band) observations by Capetti et al. (1993), supporting that there is very little polarized emission in the L-band coming from the region of molecular gas. Capetti et al. (1993) also reports a mean fractional polarization over the extent of the AGN of 12.1% $\pm$ 1.3, which is within two times the value of σ used in Capetti et al. (1993) of my measurement of 10.09%. My measurements for the core fractional linear polarization also agree with Morganti et al. (1997), who estimate an upper limit of 2.7%. Although the measurements found in Morganti et al. (1997) were taken at 6 cm (5 GHz, C-band) and my data were observed in the L-band, one would expect for depolarization effects to be stronger at longer wavelengths (O'Sullivan et al. 2017), leading to less polarized emission in the core in the L-band. Since Morganti et al. (1997) reports at least 4-6% more fractional polarization on the edges of the source than in the core, I can safely conclude that they also find the core depolarization effect significant.

Nyland et al. (2018) provides possible explanations for how Faraday rotation effect might arise in galaxies. These include internal Faraday rotation caused by the radio jet, helical magnetic fields near the launch point of the jet, external depolarization from magnetized plasma in a layer outside the jet, and depolarization by foreground clouds. Because NGC 3665 has suppressed star formation when comparing it with a stellar mass-SFR relation (Xiao et al. 2018), an intriguing explanation for the lack of polarized emission from the core of NGC 3665 is Faraday rotation causing internal depolarization through jet interactions with the molecular gas cloud. This excitation of the gas might make star formation less efficient and therefore lead to a lower SFR. Therefore, this may be evidence that the radio jets are suppressing the SFR in NGC 3665, as has been observed in other nearby AGNs (Alatalo et al. 2015).

5. Future Work

In the future, I will continue to study the polarization properties of NGC 3665 and how its radio jet's interactions with its molecular gas may affect its star formation. This can be done by calculating quantities like its rotation measure, creating a spatially resolved rotation measure map so I may observe how the Faraday depolarization varies over the source. This way, I can reach more robust conclusions about how interactions with the ISM may be responsible for depolarization. I will continue analyses like these in other jetted radio AGNs with molecular gas and spatially resolved polarization properties.

6. References

Alatalo, K., Davis, T. A., Bureau, M., et al. 2013, MNRAS, 432, 1796

Alatalo, K., Lacy, M., Lanz, L., et al. 2015, ApJ, 798, 31

Brentjens, M. 2014, Polarization in interferometry, https://science.nrao.edu/science/meetings/2014/14th-synthesis-imaging-workshop/lectures-files/polarimetrybrentjens2014.pdf

Capetti, A., Morganti, R., Parma, P., & Fanti, R. 1993, A&AS, 99, 407

Cappellari, M., Emsellem, E., Krajnović, D., et al. 2011, MNRAS, 413, 813

Condon, J. J. 1992, ARA&A, 30, 575

Evans, I. N., Primini, F. A., Glotfelty, K. J., et al. 2010, ApJS, 189, 37

Fanaroff, B. L., & Riley, J. M. 1974, MNRAS, 167, 31

Heckman, T. M., & Best, P. N. 2014, ARA&A, 52, 589

Kormendy, J., & Ho, L. C. 2013, ARA&A, 51, 511

McMullin, J. P., Waters, B., Schiebel, D., et al. 2007, ASPC, 376, 127

Morganti, R., Fogasy, J., Paragi, Z., et al. 2013, Sci, 341, 1082

Morganti, R., Parma, P., Capetti, A., et al. 1997, A&AS, 126, 335

Nyland, K., Davis, T. A., Nguyen, D. D., et al. 2017, ApJ, 845, 50

Nyland, K., Harwood, J. J., Mukherjee, D. D., et al. 2018, ArXiv e-prints, arXiv: 1803.02357

Nyland, K., Young, L. M., Wrobel, J. M., et al. 2016, MNRAS, 464, 1029

Onishi, K., Iguchi, A., Davis, T. A., et al. 2017, MNRAS, 468, 4663

O'Sullivan, S. P., Purcell, C. R., Anderson, C. S., et al. 2017, MNRAS, 469, 4034

Padovani, P., Alexander, D. M., Assef, R. J., et al. 2017, A&ARv, 25, 2

Parma, P., de Ruiter, H. R., Fanti, C., & Fanti, R. 1986, A&AS, 64, 135

Perley, R. A., & Butler, B. J. 2013, ApJS, 206, 16

Rybicki, G., Lightman, A., 1986, Radiative Processes in Astrophysics

Xiao, M., Zhao, Y., Gu, Q., & Shi, Y. 2018, ApJ, 854, 111